Results in Engineering 25 (2025) 104477

Contents lists available at ScienceDirect

Results in Engineering

journal homepage: www.sciencedirect.com/journal/results-in-engineering

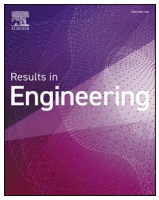

Research paper

Preliminary studies of new heat-treated titanium alloys for use in medical equipment

Cristina Jiménez-Marcos [a], Julia Claudia Mirza-Rosca [a,*], Madalina Simona Baltatu [b], Petrica Vizureanu [b]

[a] Mechanical Engineering Department, Las Palmas de Gran Canaria University, 35017, Tafira, Spain
[b] Department of Technologies and Equipments for Materials Processing, Faculty of Materials Science and Engineering, Gheorghe Asachi Technical University of Iasi, Blvd. Mangeron, No. 51, 700050 Iasi, Romania

ARTICLE INFO

Keywords:
Titanium alloys
Microhardness
Corrosion
Microstructure

ABSTRACT

Titanium alloys are essential in the biomedical field due to their exceptional corrosion resistance, mechanical strength and biocompatibility, making them ideal for producing safe medical implants and devices. Novel heat treatment techniques have been developed to optimize the microstructure, mechanical, corrosion and surface characteristics of alloys in biological environments, thereby reducing internal stresses and improving passive layer formation, thus prolonging implant service life. The analyzed samples were stress relieved titanium-molybdenum alloys (Ti-15Mo) with Si additions of 0%, 0.5%, 0.75% and 1.0%. Microstructure, microhardness and corrosion behavior were studied to evaluate the potential of these alloys for use in the human body, with a particular focus on medical devices where durability, hardness and corrosion resistance are critical factors. The addition of molybdenum as a β-phase stabilizer enhanced the formation of the advantageous lamellar microstructure of α + β phases for mechanical performance. The corrosion behavior was examined in simulated body fluid (Ringer's solution) and the higher silicon content contributed to the formation of a thicker and protective passive layer, which substantially reduced the corrosion rate. The microhardness of silicon-enriched alloys under various stress conditions was higher than that of commercially pure titanium (CpTi), demonstrating their capability for better performance in biomedical applications.

1. Introduction

The materials used for load-bearing dental and orthopedic applications must demonstrate not only excellent biocompatibility but also good mechanical properties (fatigue, tensile, compressive, elastic modulus, etc.) in conjunction with adequate ductility, hardness, and fracture toughness. Consequently, metallic implant biomaterials are more advantageous and appropriate for these applications compared to conventional ceramic and polymeric biomaterials [1]. In orthopedic and vascular surgery, classical alloys, such as Ti6Al4V, CoCrMo alloys and NiTi alloys, account for approximately 95% of orthopedic devices and 80% of implants [2].

However, special problems arise when metallic implants are used. First, the elastic modulus of metals is significantly higher than that of bone; this can lead to osteoporosis. In addition, many metallic biomaterials have some limitations in terms of biocompatibility, wear resistance, and corrosion resistance, and they release toxic ions into nearby tissues. In an attempt to solve these problems, various alloying elements that are not harmful to the body have been investigated [3,4].

Titanium and its alloys have become biomaterials that can be used for a wide range of purposes, from modern medicine to aerospace. Due to its biocompatibility [5], corrosion resistance [6], thermal stability [7], low modulus of elasticity [8], excellent fatigue resistance [9], high strength and low weight contribute to efficiency and performance in their use for biomedical applications. Titanium's exceptional corrosion resistance is attributed to its ability to build a stable oxide layer, primarily made up of titanium oxide (TiO_2) [10,11].

Nonetheless, commercial titanium alloys have distinct drawbacks when used in medical settings. The Ti-6Al-4V alloy, used to manufacture orthopedic and dental implants, may induce allergies and illnesses such as Parkinson's or Alzheimer's due to its aluminum and vanadium content [12,13]. Because it can revert to its natural form, TiNi (nitinol), which is perfect for vascular stents and guides in minimally invasive surgery, can release nickel, which can lead to both allergies as well as

* Corresponding author.
E-mail address: julia.mirza@ulpgc.es (J.C. Mirza-Rosca).

https://doi.org/10.1016/j.rineng.2025.104477
Received 20 December 2024; Received in revised form 21 February 2025; Accepted 23 February 2025
Available online 24 February 2025
2590-1230/© 2025 The Authors. Published by Elsevier B.V. This is an open access article under the CC BY-NC-ND license (http://creativecommons.org/licenses/by-nc-nd/4.0/).

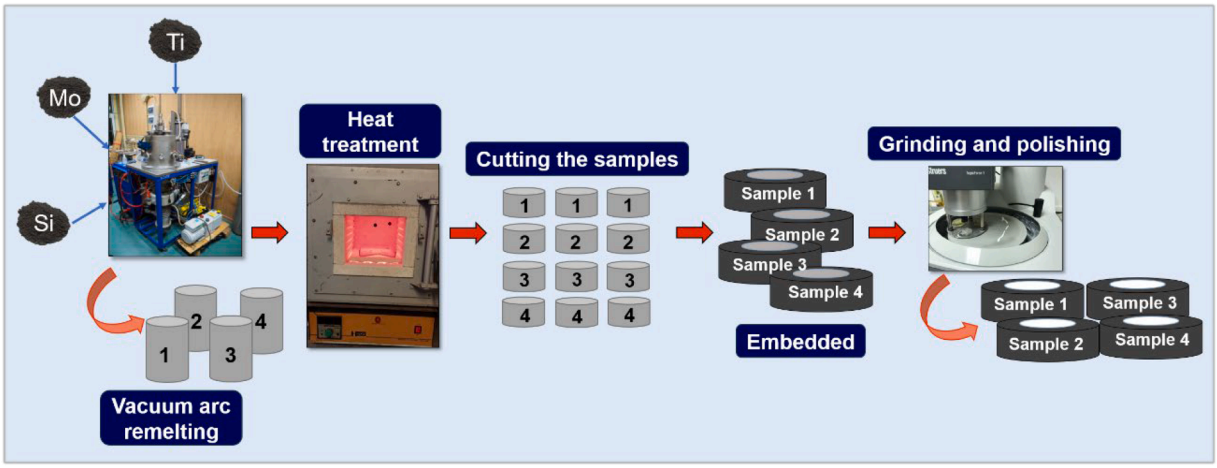

Fig. 1. Studied alloys preparation.

kidney and cardiovascular problems [14,15]. Ti-6Al-7Nb alloy, which is utilized in prostheses and medical equipment, was designed to increase biocompatibility by replacing V with Nb; nonetheless, it has a solid protective layer and presents improved mechanical properties [16,17].

The addition of highly biocompatible alloying elements such as molybdenum, helps improve the properties of titanium. Molybdenum is a low-toxicity, beta-stabilizing element that when combined with titanium, it produces a stable oxide film, shielding it from corrosion and deterioration in harsh settings [18]. Because of the high melting temperatures of the components that form the titanium-molybdenum system, the method used to obtain these alloys was vacuum arc remelting. The advantages of using this type of equipment are, in addition to the manufacture of metallic alloys with variable geometry and containing elements with very high melting temperatures, the obtaining of almost pure metallurgical environments by successive argon purging, a good homogeneity of the alloys by melting several times on each side of the ingots and the possibility of obtaining rapid water cooling [19].

In order to improve the properties, other different elements were added to Ti-Mo alloys like Zr [20–22], Nb [23], Fe [24], Cr [25], Cu [26], Au [27], Al [28], V [29], etc. The human body contains silicon, which can enhance biocompatibility and assist in controlling a material's mechanical characteristics [30,31]. Silicon (Si) can be present as a solid solution and/or silicide and even the Si content is typically restricted to below 0.5 wt%, however vacuum metallurgy demonstrates the capability to produce titanium alloys with elevated Si levels. The incorporation of silicon enhances the creep resistance, strength and oxidation resistance of titanium alloys; nevertheless, it diminishes fluidity, particularly at ambient temperature [32,33].

Heat treatment is used to minimize the residual tensions that are created during the fabrication process of titanium and titanium alloys. This process is known as stress relieving and through the use of this technique, residual stresses that are caused by the various stages of manufacturing are reduced, which helps to maintain shape stability and eliminates unfavorable situations such as the Bauschinger effect.

In this study, we focused on the effect of silicon addition on the microstructure and corrosion resistance of stress-relieved titanium alloys. The analyzed samples were titanium-molybdenum alloys with Si additions of 0%, 0.5%, 0.75% and 1.0%. The corrosion behavior was investigated to assess their performance in simulated body fluid. In addition to corrosion testing, this study aims to investigate the microstructure and microhardness behavior of these alloys. This research aims to assess the potential of these materials for use in the human body, with a particular focus on medical devices where durability, hardness and corrosion resistance are critical factors.

2. Materials and methods

2.1. Material preparation

The following alloys were produced in a vacuum arc remelting (VAR) furnace from pure alloying elements (Ti, Mo and Si): Sample 1 (85% Ti, 15% Mo), Sample 2 (84.5% Ti, 15% Mo, 0.5% Si), Sample 3 (84.25% Ti, 15% Mo, 0.75% Si), and Sample 4 (84% Ti, 15% Mo, 1% Si). In order to achieve the required homogeneity, the four alloys were subjected to a total of six remelting operations, with three repetitions on each side, under the protection of high-purity argon gas. The samples were heat treated for stress relieving at 900 °C with a heating rate of 10 °C per minute and then quenching in water.

A series of preliminary operations were conducted on the samples, including cutting with a precision saw and embedding them in epoxy resin with a catalyst mixture, followed by demolding after 24 hours. Afterward, the specimens were ground and polished at 150 rpm and 15 N of force utilizing the polishing equipment. Carbide abrasive sheets of increasing grit were used, starting with P400 grit and ending with P2500 grit [34]. Then, mirror polishing cloths containing a 0.06 μm colloidal silica polishing suspension were used (see Fig. 1). These metallographic analysis sample preparation techniques complied with ASTM E3–11 (2017) [35].

2.2. Microstructural characterization

The microstructure of the samples was examined by taking micrographs of the surfaces of each sample using an optical microscope (AxioVert.A1 MAT ZEISS) at various magnifications. For approximately 40 ss, each sample was immersed in Kroll's reagent solution, which consists of 100 ml of water, 1–3 ml of hydrofluoric acid and 2–6 ml of nitric acid. The surface that had been exposed to the reagent was then analyzed and the test was repeated three times for each sample.

An energy-dispersive X-ray spectrometer (EDX) coupled with an Apreo Field Emission scanning electron microscope was utilized for elemental analysis.

A Malvern-Panalytical diffractometer was employed for phase analysis of the samples. A CuK radiation (1.5406 Å) in the range of $2\theta = 30–70$ was used for the investigation, with a power of 45 kV, a step size of 0.02° and a current of 40 mA.

2.3. Microhardness test

In accordance with ISO 14,577–1:2015 [36], ten measurements were taken with the hardness tester Future Tech FM-810, each lasting 15 ss, for each load applied to the specimen—in this case, 5, 25 and 50 gf. As

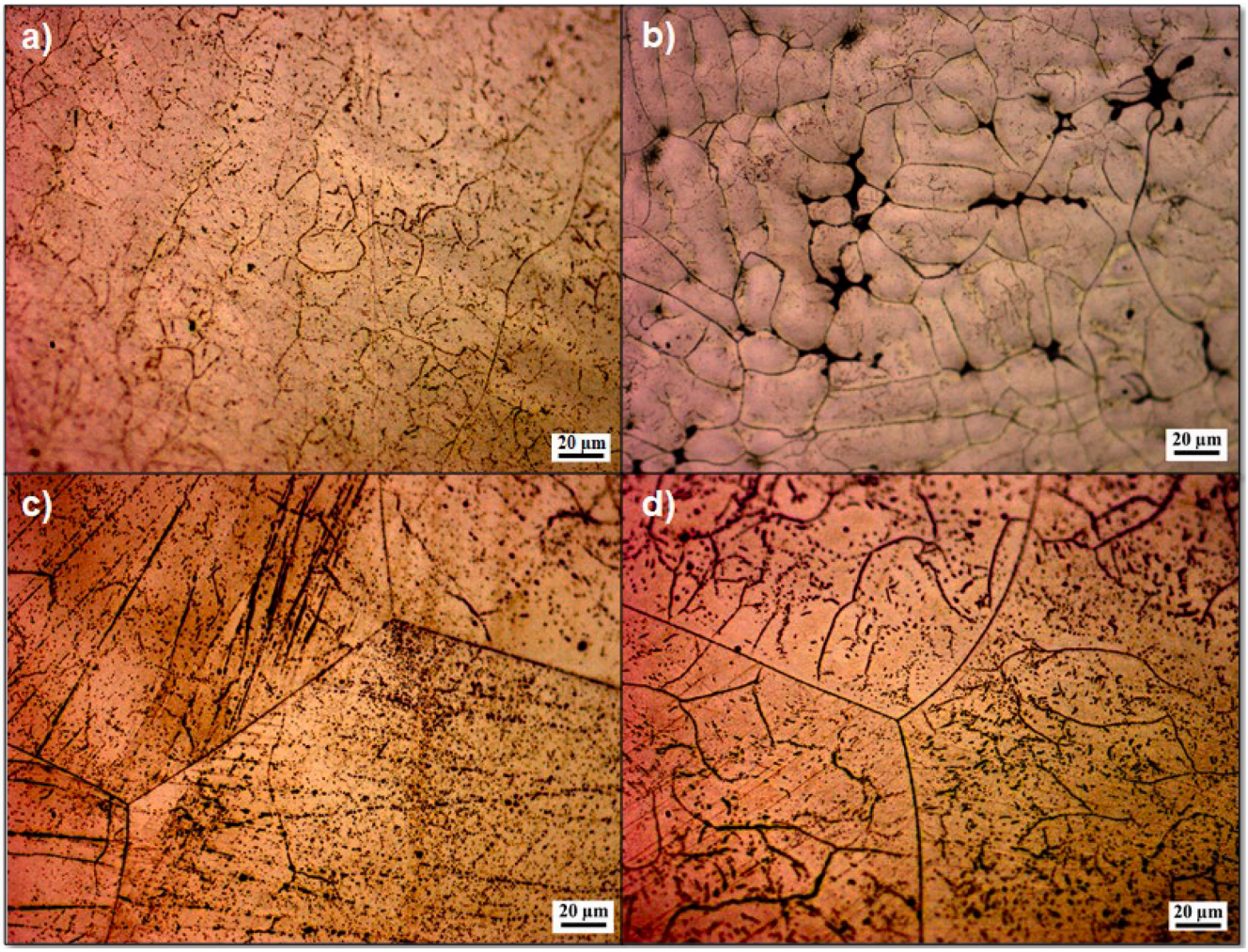

Fig. 2. Optical microstructure of: a) Sample 1, b) Sample 2, c) Sample 3 and d) Sample 4, after reagent etching.

the load increases, the impression left by the indenter can cover parts of different phases, thereby providing an approximate measure of the overall hardness of the material. The footprint can only be identified in one phase when relatively low loads are positioned, allowing the hardness of that phase to be evaluated. Subsequently, the corresponding software used the recorded diagonal lengths to automatically calculate the Vickers microhardness values. The number of indentations produced was plotted against the scan length.

2.4. Electrochemical tests

The electrochemical tests employ a three electrodes cell containing the working electrode (the material being tested), the reference electrode (saturated calomel) and the counter electrode (platinum electrode), according to ISO 10,271:2020 [37]. To conduct the tests, the area of each sample under investigation was measured. The following components were measured in mmol/L in the Ringer Grifols solution: Na^+ 129.90, Cl^- 111.70, K^+ 5.40, Ca^{2+} 1.80; and $C_3H_5O_3$ 27.20. Using the potentiostat-galvanostat SP-150 BioLOGIC, three tests were employed in the following order to study the corrosion behavior of the alloys: corrosion potential, linear polarization and electrochemical impedance spectroscopy.

2.4.1. Corrosion potential (E_{corr})

The "E_{corr} vs. Time" technique of the EC-Lab software was used to evaluate the corrosion potential of each sample after 24 hours of immersion in Ringer solution. Potential measurements were made every 300 ss or whenever the potential changed by 200 mV, conditions that, according to our previous experience [38], are sufficient to stabilize the corrosion potential as much as possible.

2.4.2. Linear polarization

To conduct these tests, the "Linear Polarization" technique was chosen, and its feasibility was confirmed by entering the sample surface area value, the 20-minute test duration and performing it three times for each sample. The used parameters were apreliminary scan rate of 0.167 mV/s, potential ranging from -1.0 to 2.0 V with respect to the reference electrode and data collected at 0.50 s intervals. Following the display of these linear polarization curves, the corrosion rate (V_{corr}) was calculated for each sample using the "Tafel Fit" approach.

2.4.3. Electrochemical impedance spectroscopy (EIS)

To characterize the oxide layer by EIS, impedance spectra were registered in the range of ±300 mV vs. E_{corr} with a step of 100 mV by continuously polarizing the sample and allowing the system to equilibrate for 600 s at each potential following ISO 16,773–1–4:2016 [39]. All the tests were normally repeated three or four times to ensure that they presented reasonable reproducibility. The data were displayed using Nyquist and Bode diagrams and an equivalent circuit (EC) was employed to fit the experimental data.

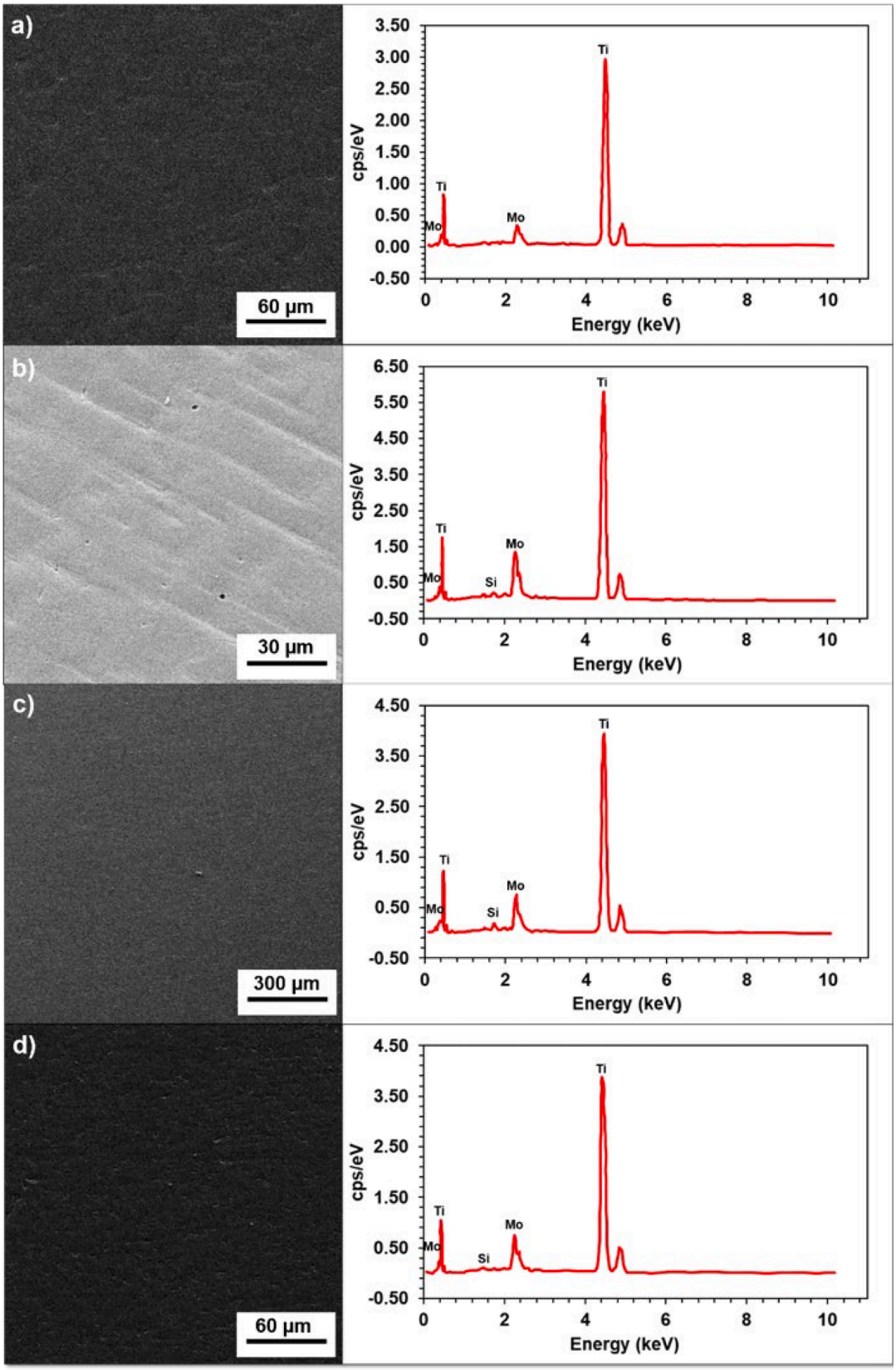

Fig. 3. SEM image and EDX spectra for: a) Sample 1, b) Sample 2, c) Sample 3 and d) Sample 4.

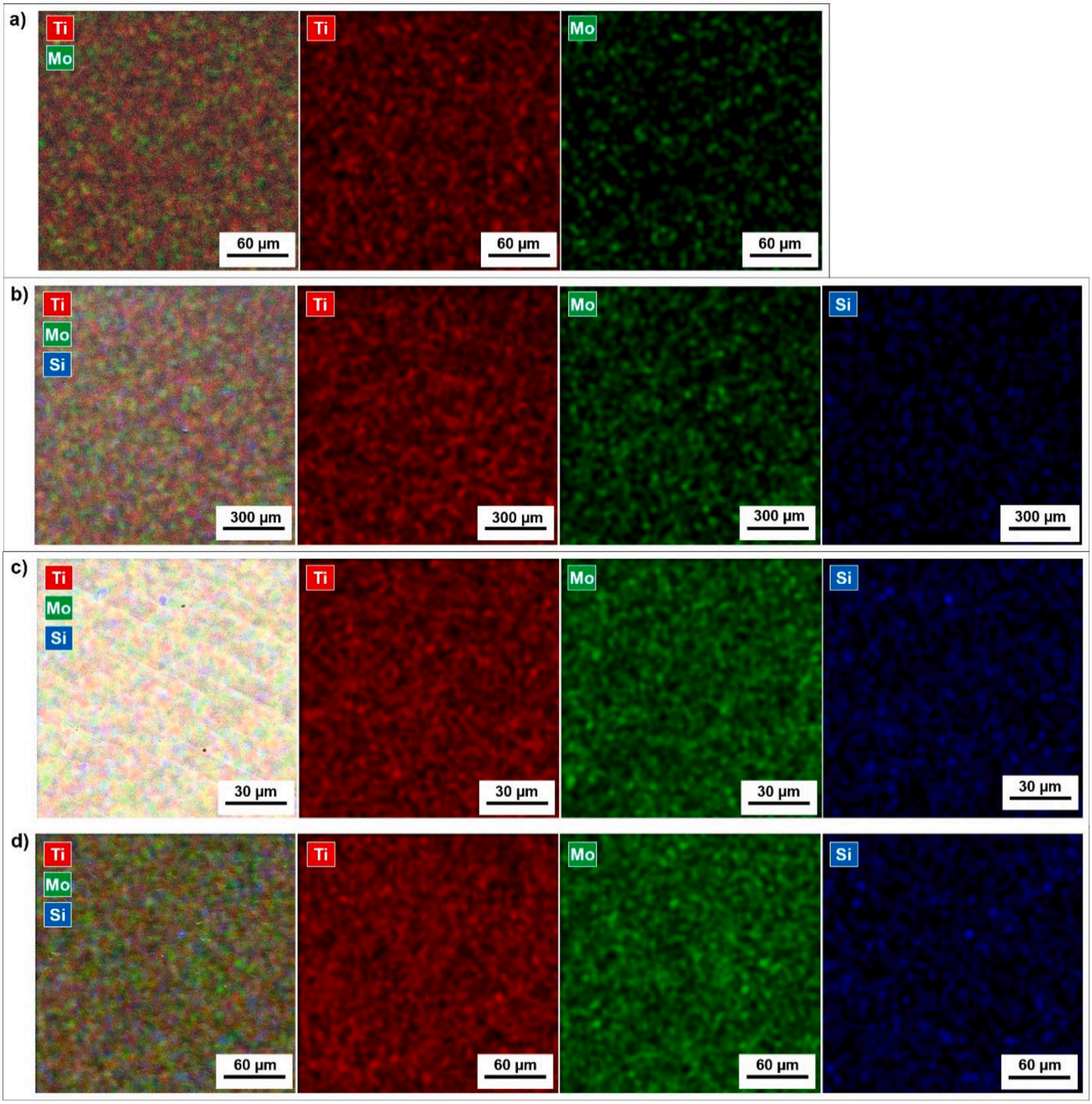

Fig. 4. EDX elemental maps of: a) Sample 1, b) Sample 2, c) Sample 3 and d) Sample 4.

3. Results and discussions

3.1. Microstructural investigation

Due to the similarity of their lattice characteristics and crystal structures, Mo and Ti can completely dissolve in one another, resulting in optimal undercooling. This facilitates the formation of the β metastable phase at elevated temperatures [40]. The β-phase (BCC structure) is achieved by including the transition components Mo and Si.

Silicon can reduce the phase transition temperature because it is an eutectoid β-stable element and typically exists as a solid solution or silicide in titanium-based alloys. The various morphological forms of silicon can be interconverted under specific conditions, which enables the variation of titanium alloy properties by silicide [32]. The silicide in this case is an intermetallic compound formed between silicon and titanium.

The optical microscope images of the four samples, as presented in Fig. 2, illustrate the microstructural changes occurring with varying silicon concentrations. At lower silicon concentrations, it can be observed that the precipitation of silicide begins near the grain boundaries of the β-phase (see Fig. 2a). As silicon concentrations increase, silicide precipitation is seen to begin within the crystal structure itself (refer to Figs. 2a and 2b). These observations align with established patterns reported in the literature [41,42], where similar behavior has been noted under comparable conditions.

Figs. 3 and 4 display SEM pictures, EDX spectra and EDX elemental maps for the examined area of each sample. In the presented SEM images (Fig. 3), different magnifications were employed not to emphasize

Table 1
EDX quantification of the samples analyzed.

Samples	Composition (in wt%)		
	Ti	Mo	Si
Sample 1	84.44 ± 2.35	15.56 ± 1.56	–
Sample 2	83.79 ± 1.80	15.93 ± 1.23	0.28 ± 0.08
Sample 3	83.84 ± 2.02	15.30 ± 0.98	0.86 ± 0.16
Sample 4	83.79 ± 2.11	15.19 ± 1.61	1.02 ± 0.34

microstructural clarity but to optimize the surface details necessary for detailed elemental analysis by EDX. These magnifications were selected based on the need to effectively capture compositional variations that could not be adequately represented at a single scale.

The quality of the SEM images, as presented in our study, differs from that of the optical microscope images (see Fig. 2) due to the specific objectives of each imaging technique. Unlike optical imaging, which focuses on microstructural clarity, the SEM images were specifically optimized for the comprehensive elemental analysis essential for our research. This optimization was targeted at enhancing the accuracy of EDX data rather than visual detail, which is critical to the goals of our study.

The EDX quantification provides a summary of the mean chemical compositions of the alloys researched (see Table 1), which demonstrates a close agreement with the theoretical concentrations of the chemical elements, with only slight differences due to local inhomogeneities or measurement uncertainty. The presence of SiO_2 has been identified by EDX, a method that is essential not only for the detection SiO_2 but also for confirming the integration of silicon in the passive films, which correlates with the varying silicon content in the different samples: Sample 1 without Si, Sample 2 with 0.5% Si, Sample 3 with 0.75% Si and Sample 4 with 1% Si.

The silicon content in these alloys plays an important role in enhancing the formation and stability of SiO_2 within the passive films. As the percentage of silicon increases from 0.5% to 1%, we observed an improvement in the compactness and stability of the film, which can be directly attributed to a higher concentration of SiO_2. This enhancement is supported by the literature [43,44] indicating that SiO_2 effectively improves the corrosion resistance and mechanical properties of protective films.

The generated atomic distribution maps (see Fig. 4) provide clear evidence of the absence of elemental segregation or the connection of impurities within the alloy matrix. By confirming the lack of inclusions and segregations, we can infer that the alloy processing methods used were effective in achieving a homogeneous material structure. This homogeneity indicates higher material integrity and predictability of clinical performance.

The diffraction diagrams of the alloys being studied are shown in Fig. 5. Only two phases—major β and minor Ti_5Si_3—were discernible in this instance. It is evident that all alloys present significant peaks that correlate with the titanium β phase. Silicon and molybdenum, two alloying elements added to titanium, are β-stabilizers, meaning they prevent other phases from precipitating [45]. Our X-ray diffractograms support the equivalent molybdenum hypothesis, according to which, at room temperature, the predominance of the β-phase requires the use of at least 10 wt% molybdenum [46].

3.2. Microhardness test

Fig. 6 and Table 2 show the microhardness results at HV 0.005, HV 0.025, and HV 0.05, together with the mean, median, standard deviation (SD), minimum, maximum and depth values for each of the ten indentations performed on each sample. As can be seen, there is little variation in the data and a mean of about 350 HV for the values applied in Samples 1, 3 and 4. Sample 3 displayed the highest values for the applied loads of 5 and 25 gf; however, Sample 4 displayed a higher value when the load of 50 gf was applied. On the other hand, Sample 3 provided the lowest hardness value for the 5 gf load, while Sample 1 provided the minimum values for the other two charges. However, it is difficult to determine whether the proportion of silicon increases or decreases, as the data shows that the surfaces of both samples are somewhat uniform. Sample 2, on the other hand, showed Vickers hardness values with a considerable variance, ranging from 290 to 530 HV and a standard deviation of 55 to 77, suggesting the existence of hard

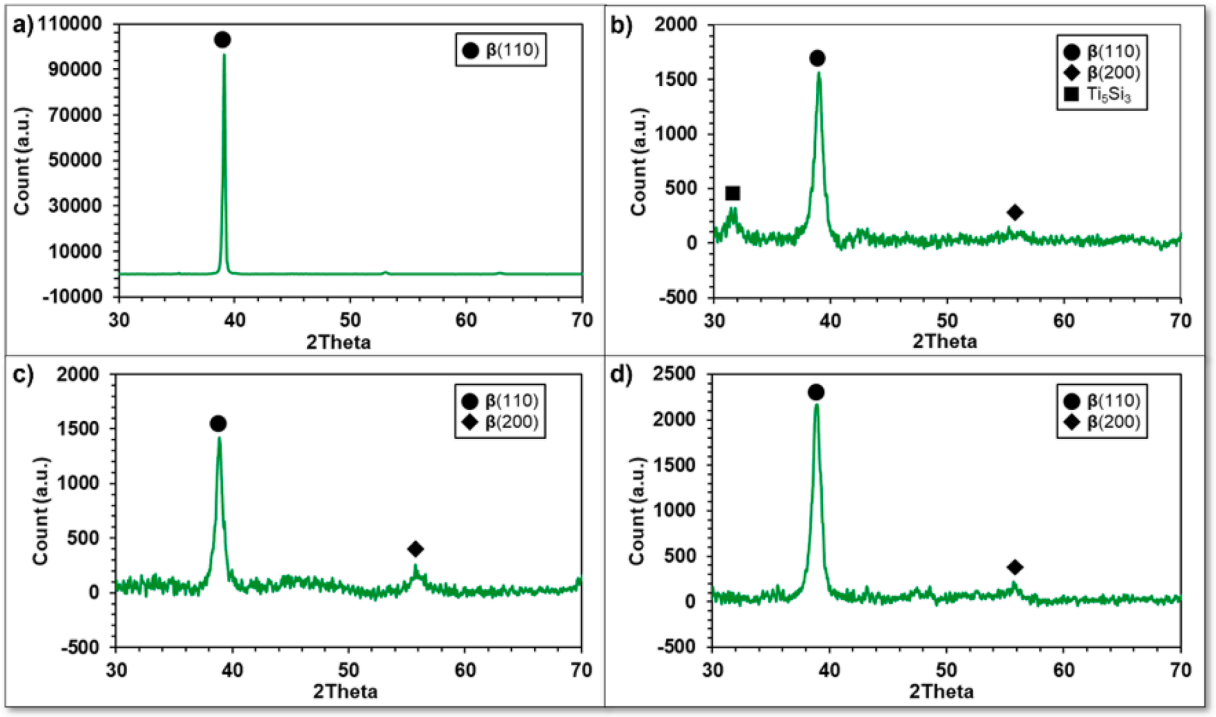

Fig. 5. X-ray diffraction (XRD) pattern of the studied alloys: a) Sample 1, b) Sample 2, c) Sample 3 and d) Sample 4.

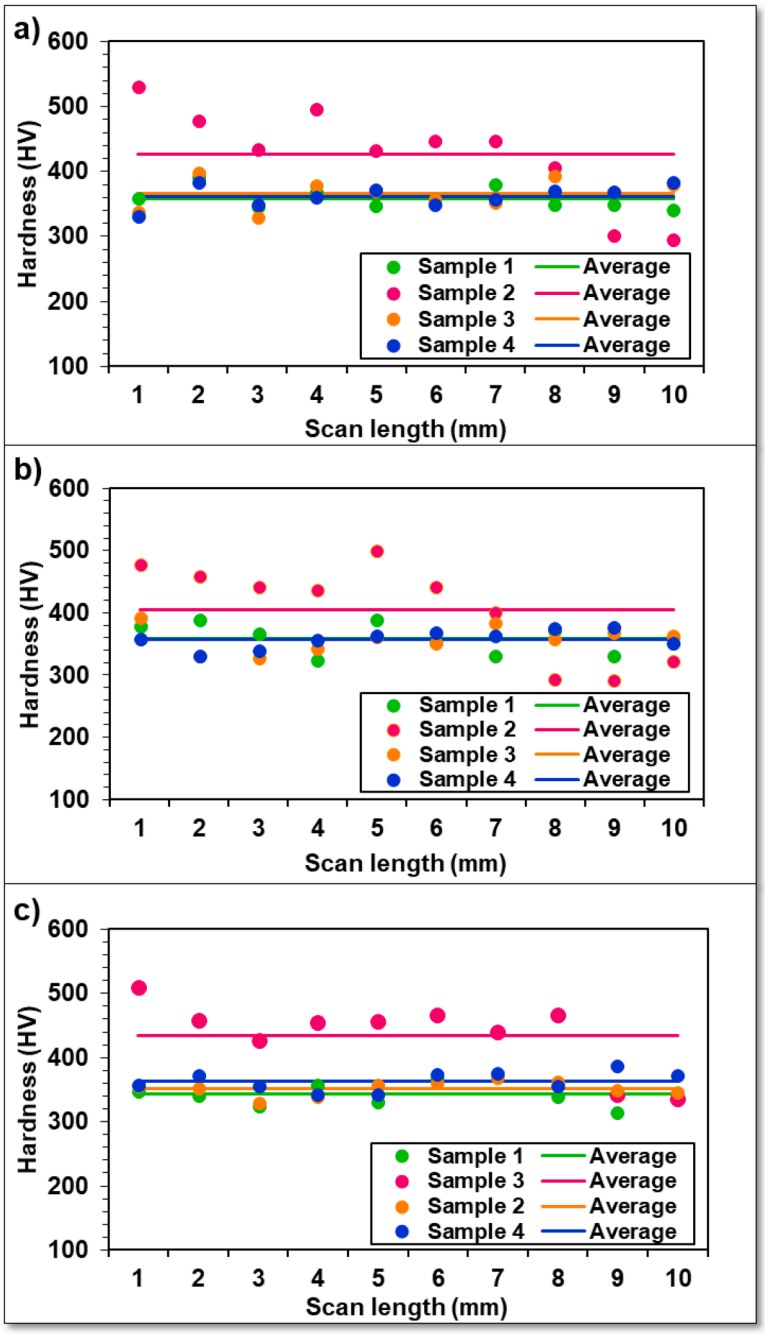

Fig. 6. Microhardness results for each indentation for the test specimens under loadings of 5 (a), 25 (b) and 50 (c) gf.

and soft zones (different phases) on its surface.

Additionally, the maximum hardness values found in this study were higher than those of cp-Ti (180 - 300 HV) [47,48] but lower than those of Ti6Al4V (330 - 540 HV) [49,50].

The SD of all specimens tends to decrease at higher loads since the higher the load, the greater the penetration into the material. This fact can be demonstrated by calculating the thickness of the footprint.

The following formula is used to calculate the depth of the indentation, where F is the applied force in kgf and HV is Vickers hardness in kgf/mm^2.

$$\delta = 0.202 \cdot \sqrt{\frac{1.8544 \cdot F}{HV}} \quad (1)$$

Because the hardness levels of the materials were equal, when a higher load was applied, the average depth of the footprint rose from 0.9 μm to 3.3 μm.

As established by the Hall-Petch relationship, the microhardness of materials can be improved by grain refinement [51]. The grain sizes of Sample 2 are significantly refined compared to those of the other samples, thereby increasing the microhardness. The precipitation of silicide at the boundary of the crystal generates a big difference between the maximum and minimum values of the microhardness, depending on the phase. For samples 2 and 3, due to their homogeneity and the uniform silicides inside the crystals, the microhardness values are kept at roughly the same levels.

3.3. Electrochemical tests

3.3.1. Corrosion potential

The corrosion potential versus time curves of the studied samples

Table 2
Microhardness values and depth of the four samples for 5, 25 and 50 gf.

Essay		Microhardness (HV)					Depth (μm)
		Mean	Median	SD	Maximum	Minimum	
Sample 1	5 gf	358	353	16	390	340	1.03
	25 gf	358	363	24	388	323	2.30
	50 gf	343	342	18	368	314	3.32
Sample 2	5 gf	426	440	76	530	294	0.94
	25 gf	405	438	77	498	290	2.16
	50 gf	435	455	55	509	335	2.95
Sample 3	5 gf	366	368	23	397	328	1.02
	25 gf	357	359	21	392	326	2.30
	50 gf	351	354	12	368	328	3.28
Sample 4	5 gf	361	363	16	382	330	1.02
	25 gf	357	360	15	376	330	2.30
	50 gf	363	364	15	386	341	3.23

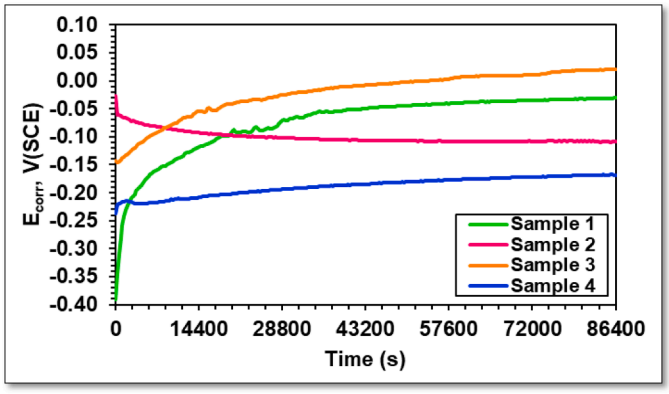

Fig. 7. Corrosion potential curves for the four samples after 24 hours' immersion time.

Table 3
Results of the corrosion potential for the investigated samples submerged in Ringer Grifols electrolyte at the beginning, 2 hours later, 12 hours later, and 24 hours later.

Potential (V)	Sample 1	Sample 2	Sample 3	Sample 4
Initial	-0.345	-0.062	-0.147	-0.221
After 2 hours	-0.159	-0.082	-0.093	-0.217
After 12 hours	-0.050	-0.106	-0.007	-0.185
After 1 day	-0.031	-0.108	0.021	-0.168

were analyzed after a 24-hour testing period during which the samples were immersed in Ringer's solution (see Fig. 7 and Table 3). Under these circumstances, the potential—known as the open circuit potential, or OCP—indicates the sample's propensity to resist corrosion.

Thus, immersing the alloys in Ringer's solution for 24 hours showed that the four samples had a high qualitative tendency to passivate.

Table 3 shows that the initial potential values of the samples tend to increase with the addition of silicon. From the data collected during the first two hours of immersion, Sample 1, Sample 3 and Sample 4 reached more positive values between -0.345 V and -0.093 V, while Sample 2 suffered a slight drop in the potential from -0.062 V to -0.082 V. Subsequently, after 12 hours, Sample 2 continues to reach more negative potential values to reach -0.106 V. Nevertheless, the potential of the rest

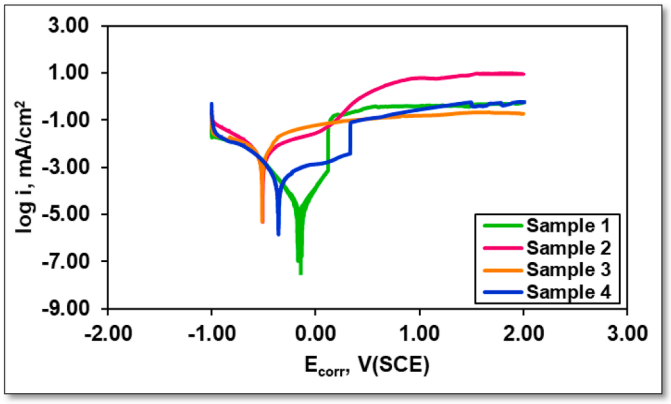

Fig. 8. Polarisation curves of the four test samples.

Table 4
Corrosion parameters obtained for all samples tested.

Parameters	Sample 1	Sample 2	Sample 3	Sample 4
E_{corr} (mV vs. Ref)	-260 ± 2	-138 ± 1	-239 ± 2	-69 ± 2
I_{corr} (μA/cm²)	$7.60 \cdot 10^{-4}$	$3.00 \cdot 10^{-1}$	$3.00 \cdot 10^{-3}$	$3.00 \cdot 10^{-3}$
β_c (mV/dec)	14.5 ± 1.3	14.9 ± 2.1	4.5 ± 1.7	4.1 ± 1.9
β_a (mV/dec)	35.3 ± 2.4	26.4 ± 2.7	32.3 ± 2.6	143.2 ± 3.5
Equivalent weight (g/eq)	23.94	23.52	23.66	23.38
Density (g/cm³)	5.36	5.34	5.35	5.34
Surface (cm²)	1.00	1.10	1.08	1.12
Corrosion rate (mpy)	$4.39 \cdot 10^{-3}$	$1.56 \cdot 10^{-1}$	$2.12 \cdot 10^{-3}$	$1.52 \cdot 10^{-3}$
R_p (MOhm·cm²)	2.84 ± 0.32	1.18 ± 0.06	1.22 ± 0.47	2.10 ± 0.24

of the samples in the study continues to increase. At the end of the test, positive behavior can be observed for all the samples, because they tend to achieve a certain stability. For the examined samples, the constant movement of the potential towards noble values suggested that the passive layer underwent modifications during the testing, becoming more protective. The Si content can influence the stability, thickness and composition of the passive oxide layer formed on the alloy surface.

3.3.2. *Linear polarization*

Fig. 8 and Table 4 illustrate the outcomes of the linear polarization technique employed to assess the corrosion rate of the alloys, presented on a semi-logarithmic scale of the actual results.

As can be observed in Table 4, Sample 4 exhibits higher anodic corrosion potential and current values (E_{corr} and I_{corr}, respectively), which indicate the extent of alloy oxidation, than the other samples examined.

To determine the Tafel slopes (β_c and β_a), the curve was examined against reference potential throughout a range of -1.0 to 2.0 V. A value of βa larger than βc indicates an alloy that is prone to passivation, whereas a value of β_a less than β_c indicates an alloy that is prone to corrosion. In this instance, the analysis revealed a propensity for all four samples to undergo passive layer formation on their surface [52].

Additionally, as illustrated in Table 4, the Tafel curve parameters and the corrosion rate (V_{corr}) of the tested samples are presented. These are determined using the corrosion current (I_{corr}), the density (d) in g/cm³, the area (A) of each sample (in cm²), the equivalent weight (EW) in g/eq and the constant (K) that determines the corrosion rate units (1.288·105 milinches/A-cm-year). The equivalent weight was calculated for each sample applying the following formula, which is from the standard ASTM G102–23 [53]:

$$EW = \frac{1}{\sum \frac{nifi}{Wi}} \quad (2)$$

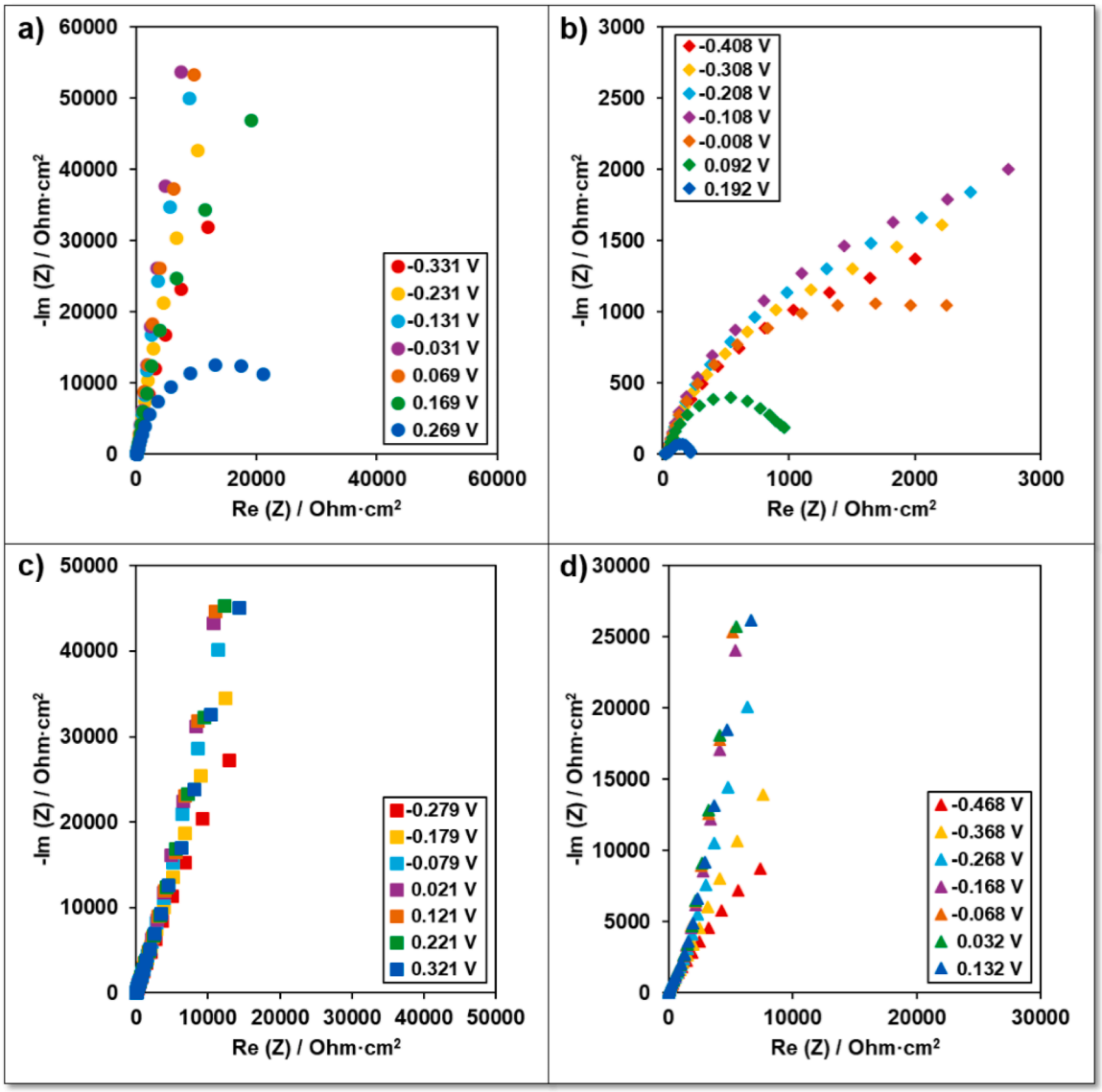

Fig. 9. Nyquist diagrams of: a) Sample 1, b) Sample 2, c) Sample 3 and d) Sample 4.

Where ***Wi*** is the atomic weight of the ith element in the alloy, ***ni*** is its valence, and ***fi*** is its mass fraction in the alloy.

In this case, a minimum V_{corr} of $1.52{\cdot}10^{-3}$ mpy was reached for Sample 4 and a maximum V_{corr} of $1.56{\cdot}10^{-1}$ mpy for Sample 2. Ti-6Al-4V and cp-Ti, under similar circumstances, showed a higher corrosion rate of about 10^{-2} mpy [50,54].

As the polarization resistance (R_p) value increases, the corrosion resistance of the alloy also improves, as shown by the results of the "R_p Fit" study. Sample 1, Sample 3 and Sample 4 exhibit an extremely high degree of corrosion resistance, with R_p values reaching as high as 10^6 $\Omega{\cdot}cm^2$ for highly corrosion-resistant materials. In this case, the R_p values achieved for these ssamples were higher than those obtained for cp-Ti (10^5 $\Omega{\cdot}cm^2$) [48], except for Sample 2, which has a R_p of 10^4 $\Omega{\cdot}cm^2$.

3.3.3. *Electrochemical impedance spectroscopy*

Figs. 9, 10 and 11 show the Nyquist and Bode impedance and Bode phase diagrams obtained for seven applied potentials (±0.3 V vs. reference electrode (E_{ref})) of each sample from high to low frequencies (200 KHz – 0.1 Hz).

Analyzing the Nyquist plot in Fig. 9, which shows the imaginary impedance versus the real impedance, Sample 1 and Sample 3 have similar impedance values for their E_{corr} (at 0.0 V vs. E_{corr}), slightly superior for Sample 1, which indicates a larger arc and is therefore more capacitive. There is also a tendency for the impedance values of Sample 3 and Sample 4 to increase at more positive potentials, while the impedance values of Sample 1 and Sample 2 exhibit a decrease in response to higher potentials (from 0.2 to 0.3 V vs E_{corr}).

In the Bode-IZI diagrams presented in Fig. 10, at high and medium frequencies, the impedance spectra exhibit similar curves. However, at a low frequency of 0.1 Hz, a flat surface impedance is observed, representing the sum of surface layer resistance, transfer resistance, and electrolyte resistance. This is associated with the inherent quality of the protective film.

In this instance, the impedance values obtained for Sample 3 and Sample 4 exhibited an increasing trend as more positive potentials were applied during the test, while Sample 1 and Sample 2 reached their maximum values at 0.0 V against E_{corr}. In this scenario, Sample 1 achieved the maximum impedance.

As demonstrated in Fig. 11 and Table 5, the Bode phase diagrams illustrate the phase transition as a function of frequency for varying potentials in comparison to the reference electrode. It is evident from the data that the maximum values of the phase angle occur when the corrosion potential is applied, with Sample 1 demonstrating higher values. Furthermore, the process occurs in two or three stages (time

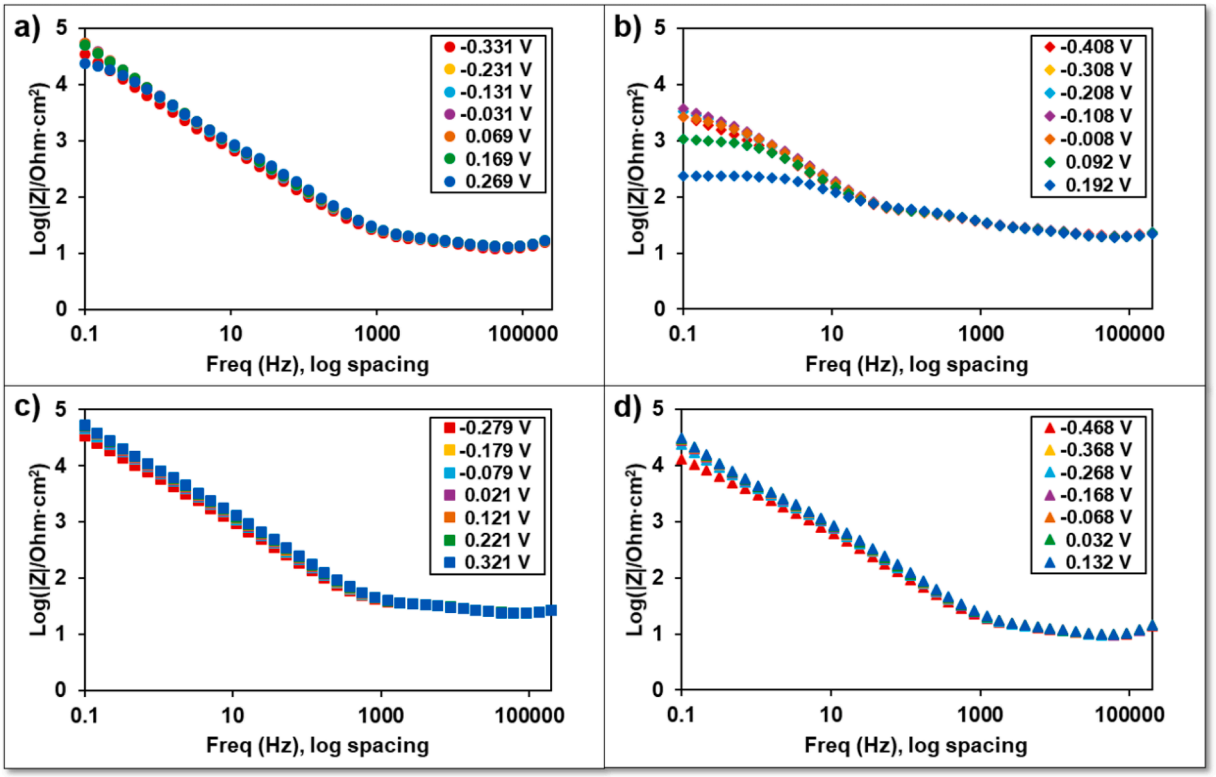

Fig. 10. Bode-impedance diagrams of: a) Sample 1, b) Sample 2, c) Sample 3 and d) Sample 4.

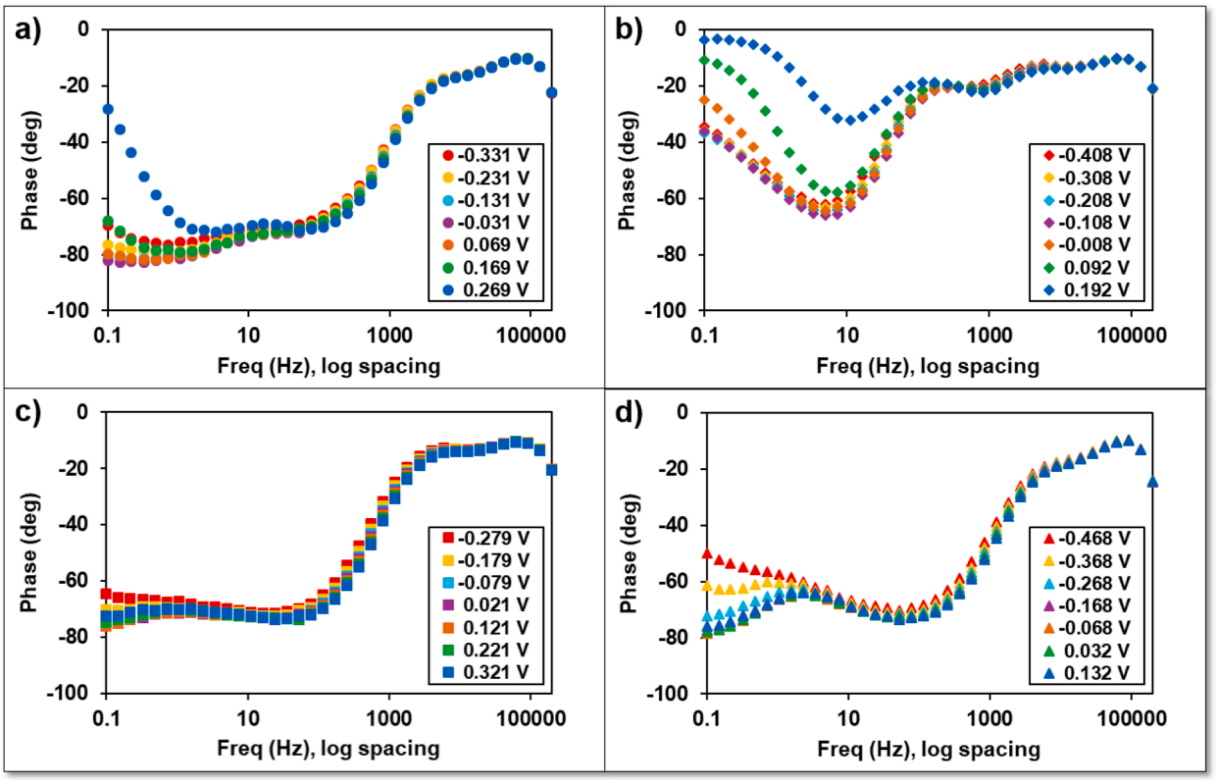

Fig. 11. Bode-phase diagrams of: a) Sample 1, b) Sample 2, c) Sample 3 and d) Sample 4.

constant) as the curve angles towards lower frequencies. The maximum phase angle is centered at approximately 10 Hz for Sample 2 and 100 Hz for Sample 1, Sample 3 and Sample 4. Furthermore, an increase in the response of the phase angle values of Samples 3 and 4 is observed at more positive potentials, indicating a transition from a capacitive to a resistive film. In contrast, the impedance values of Samples 1 and 2 show

Table 5
Results from the Bode plots of the samples studied at different potentials (±0.3 V vs. E_{corr}).

Parameters	Sample 1	Sample 2	Sample 3	Sample 4
Potential (V)	-0.331	-0.408	-0.279	-0.468
Max impedance (Ω·cm²)	34,044.51	2424.45	30,218.44	11,418.86
Max phase angle (°)	76.05	62.02	71.44	69.28
Potential (V)	-0.031	-0.108	0.021	-0.168
Max impedance (Ω·cm²)	54,279.79	3391.53	44,615.95	24,646.11
Max phase angle (°)	82.73	66.10	76.05	77.31
Potential (V)	0.269	0.192	0.321	0.132
Max impedance (Ω·cm²)	23,939.60	221.38	47,380.15	27,010.55
Max phase angle (°)	72.08	32.09	73.72	75.77

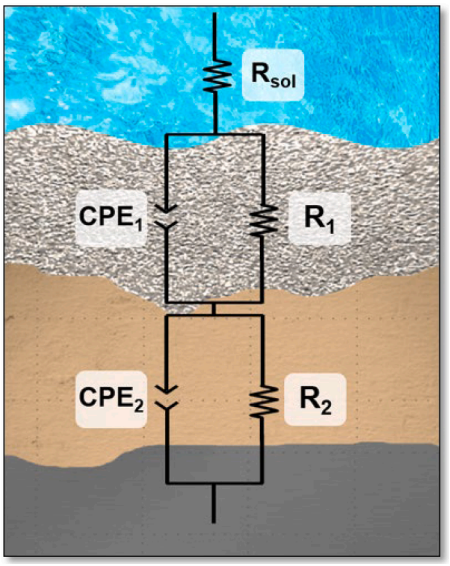

Fig. 12. Equivalent circuit $R_{sol}(CPE_1\ R_1)(CPE_2\ R_2)$ applied for the studied samples.

a decrease in response to higher potentials (0.2 to 0.3 V vs. E_{corr}).

It is evident that corrosion resistance is dependent on impedance and phase angle values, with Sample 1 demonstrating notable resistance and Sample 2 exhibiting significantly lower values.

Fig. 12 displays the analogous circuit model R(CPE R)(CPE R) applied from the results obtained, which best fits the experimental results of the research and demonstrates that the surface of the samples is resistant to dissolution along with a double passive film (porous and compact) up until the alloy is obtained.

The model and the following equations represented the electrolyte's resistance in ohms as R_{sol}, the passive film's capacitances as CPE_1 and CPE_2 and the constant phase elements and the porous and compact passive film resistances as R_1 and R_2, respectively. The constant phase element replicates the semi-infinite Warburg impedance (n = 0.5), the resistor (n = 0.0), and the capacitor (n = 1.0) as a function of the applied frequency (f) and the values of the parameters n_1 and n_2 [55].

$$Z_{series} = Z_1 + Z_2 + Z_3 \tag{3}$$

$$\frac{1}{Z_{parallel}} = \frac{1}{Z_{CPE}} + \frac{1}{Z_R} \tag{4}$$

$$Z_{parallel} = \frac{Z_R \cdot Z_{CPE}}{Z_R + Z_{CPE}} \tag{5}$$

$$Z_R = R\ Z_{CPE} = \frac{1}{Y^0(jw)^n} \tag{6}$$

$$Z_{parallel} = \frac{R}{1 + RY^0(jw)^n} \tag{7}$$

$$Z(f) = R_{sol} + \frac{R_1}{1 + R_1 Y_1^0(jw)^{n_1}} + \frac{R_2}{1 + R_2 Y_2^0(jw)^{n_2}} \tag{8}$$

The results obtained through the application of the equivalent circuit $R_{sol}(CPE_1\ R_1)(CPE_2\ R_2)$ were found to be in accordance with the experimental data. Furthermore, the chi-squared values were of the order of 10^{-3}, thereby indicating that the simulation quality was satisfactory. The spectra obtained from EIS, when interpreted through the lens of a two-time constant equivalent circuit model, point to the presence of a two-layer passive film structure.

As in the Nyquist and Bode graphs, Fig. 13 shows the evolution of the values of different resistances and constant phase elements of the porous and compact protective layers with the seven potentials applied.

In general, resistance values tend to increase up to -0.1 V for all the samples tested, being higher R_1 for Sample 4. This finding suggests that the incorporation of silicon enhances the corrosion of the outer passive layer of the sample. Sample 1 had a stronger corrosion resistance ($R_p = R_1 + R_2$), reaching values of up to 10^3 KOhm·cm², while Sample 2 had the lowest resistance results (4 KOhm·cm² max). The R_2 values are higher than the R_1 values, which is indicative of the fact that the outer porous layer exhibits a lower resistance than the inner compact film.

In addition, Sample 1 and Sample 2 have lower resistance values as the applied voltage became more positive. This decline in resistance as the applied potential increases to positive values can be attributed to two phenomena: film thinning and breakdown at higher potentials. In contrast, Sample 3 has the maximum resistance value at 0.0V and Sample 4 at -0.1 V. Except for Sample 2, the studied samples had strong corrosion resistance since their values were between 10^4 and 10^6 Ohm·cm².

The fitted values of Y_1 and Y_2 decrease as Si concentration increases, indicating that the compactness and stability of the passive protective film have improved due to SiO_2 production.

4. Conclusions

This paper has studied four heat-treated titanium alloys that contain non-toxic and biocompatible components, such as molybdenum (Mo) and silicon (Si). The main conclusions of the study are briefly summarized below:

- The results showed that the addition of silicon to the Ti-15Mo alloy affects the homogeneity and distribution of phases. The X-ray diffraction (XRD) analysis showed the predominant presence of β phase with a smaller amount of silicide.
- It was observed that during immersion in Ringer's solution, the samples retain the stability of their potential, with the sample with 0.75%Si having a higher potential that inhibits the cyclic rupture and repassivation of the passive layer that has developed on its surface. On the other hand, it has been shown that a higher concentration of silicon (more than 0.5% Si) slows down the corrosion process because it favors the development of a more compact and effective passive layer. The corrosion rate in simulated physiological medium decreases by more than 50% with the addition of 0.75% Si and this decrease reaches 75% if the Si concentration is 1%.
- All the alloys demonstrated comparable hardness values at varying loadings, higher than those of commercial pure titanium (CpTi). When the Si addition is very low (0.5%), the formation of the silicide at the edge of the crystals generates elevated dispersion of the microhardness values due to the lack of microstructural homogeneity.

These results were largely positive for the corrosion behavior of the samples, showing that, at Si additions higher than 0.5 wt%, there was

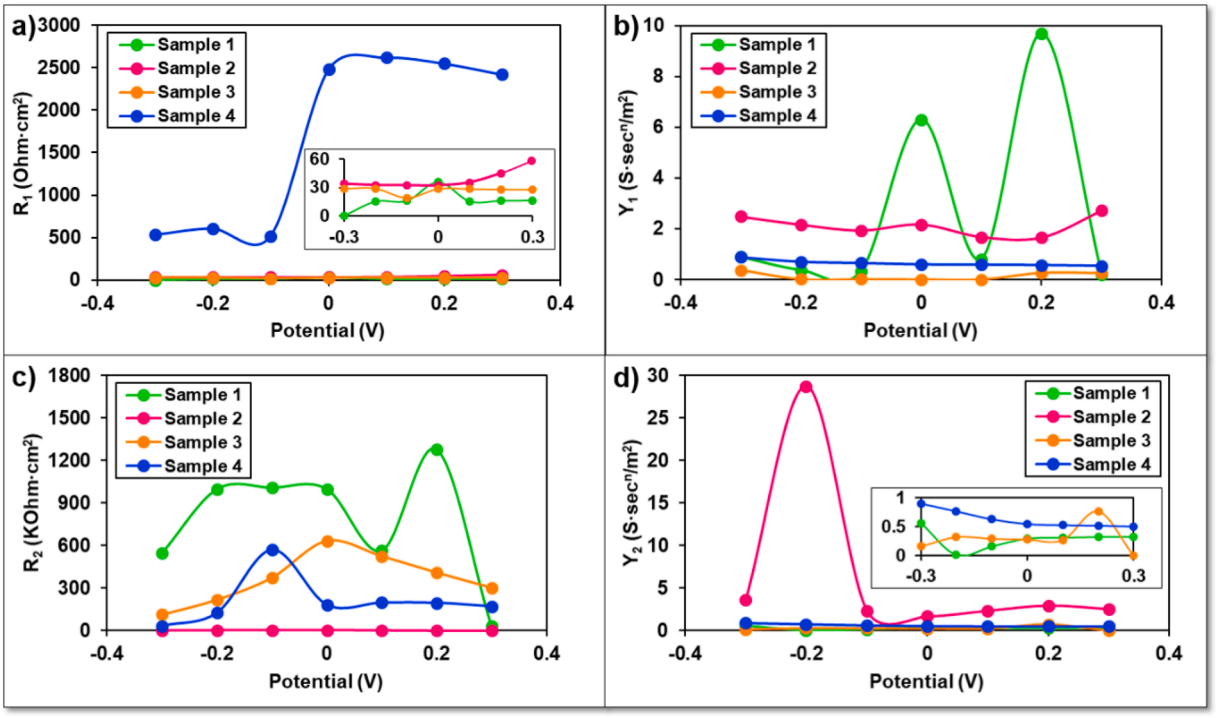

Fig. 13. Evolution of a) R_1 and b) Y_1 with the different potentials applied for the porous film, c) R_2 and d) Y_2 with the different potentials applied for the compact film of the samples studied.

very good corrosion resistance and mechanical properties similar to other commercial alloys.

CRediT authorship contribution statement

Cristina Jiménez-Marcos: Writing – original draft, Investigation, Formal analysis, Conceptualization. **Julia Claudia Mirza-Rosca:** Writing – review & editing, Methodology, Funding acquisition. **Madalina Simona Baltatu:** Resources, Investigation, Formal analysis. **Petrica Vizureanu:** Validation, Supervision, Resources, Methodology.

Declaration of competing interest

The authors declare that they have no known competing financial interests or personal relationships that could have appeared to influence the work reported in this paper.

Acknowledgements

We are grateful for the collaboration of the European project 2023–1-RO01-KA220-HED-000159985: Smart Healthcare Engineering and the Cabildo22–01 project.

Data availability

Data will be made available on request.

References

[1] D. Aggarwal, V. Kumar, S. Sharma, Drug-loaded biomaterials for orthopedic applications: A review, J. Control. Release. 344 (2022) 113–133, https://doi.org/10.1016/j.jconrel.2022.02.029.
[2] T. Hanawa, Metals and medicine, Mater. Trans. 62 (2021) 139–148, https://doi.org/10.2320/matertrans.MT-M2020268.
[3] M.K. Gouda, S.A. Salman, S. Ebied, A.M. Ashmawy, M.A.H. Gepreel, A. Chiba, Biocompatibility and corrosion resistance of low-cost Ti–14Mn–Zr alloys, J. Mater. Res. 36 (2021) 4883–4893, https://doi.org/10.1557/s43578-021-00441-w.
[4] M.K. Gouda, S.A. Salman, S. Ebied, Improvement in the microhardness and corrosion behaviour of Ti-14Mn biomedical alloy by cold working, Mater. Res. Express. 9 (2022) 015401, https://doi.org/10.1088/2053-1591/ac4b77.
[5] R.Eftekhar Ashtiani, M. Alam, S. Tavakolizadeh, K. Abbasi, The role of biomaterials and biocompatible materials in implant-supported dental prosthesis, evidence-based complement, Altern. Med. 2021 (2021) 1–9, https://doi.org/10.1155/2021/3349433.
[6] M.S. Baltatu, P. Vizureanu, A.V. Sandu, N. Florido-Suarez, M.V. Saceleanu, J. C. Mirza-Rosca, New titanium alloys, promising materials for medical devices, Materials. (Basel) 14 (2021) 5934, https://doi.org/10.3390/MA14205934.
[7] R. del Castillo, K. Chochlidakis, P. Galindo-Moreno, C. Ercoli, Titanium nitride coated implant abutments: from technical aspects and soft tissue biocompatibility to clinical applications. A literature review, J. Prosthodont. 31 (2022) 571–578, https://doi.org/10.1111/jopr.13446.
[8] Y. Fu, W. Xiao, J. Rong, L. Ren, H. Peng, Y. Wen, X. Zhao, C. Ma, Achieving large near-linear elasticity, low modulus, and high strength in a metastable β-Ti alloy by mild cold rolling, J. Mater. Sci. Technol. 189 (2024) 1–12, https://doi.org/10.1016/j.jmst.2023.11.066.
[9] E. Marin, A. Lanzutti, Biomedical applications of titanium alloys: A comprehensive review, Materials. (Basel) 17 (2023) 114, https://doi.org/10.3390/ma17010114.
[10] N. Sirdeshmukh, G. Dongre, Achieving controlled topography and wettability through laser surface texturing of Ti6Al4V for bioengineering applications, Results. Eng. 17 (2023) 100898, https://doi.org/10.1016/j.rineng.2023.100898.
[11] M.V. Popa, E. Vasilescu, P. Drob, M. Anghel, C. Vasilescu, I. Mirza-Rosca, A. S. Lopez, Anodic passivity of some titanium base alloys in aggressive environments, Mater. Corros. 53 (2002) 51–55, https://doi.org/10.1002/1521-4176(200201)53:1<51. AID−MACO51>3.0.CO;2-6.
[12] A. Azmat, S. Asrar, I.A. Channa, J. Ashfaq, I. Ali Chandio, A.D. Chandio, M. Ali Shar, M.S. AlSalhi, S. Devanesan, Comparative study of biocompatible titanium alloys containing non-toxic elements for orthopedic implants, Crystals. (Basel) 13 (2023) 467, https://doi.org/10.3390/cryst13030467.
[13] G. Khadija, A. Saleem, Z. Akhtar, Z. Naqvi, M. Gull, M. Masood, S. Mukhtar, M. Batool, N. Saleem, T. Rasheed, N. Nizam, A. Ibrahim, F. Iqbal, Short term exposure to titanium, aluminum and vanadium (Ti 6Al 4V) alloy powder drastically affects behavior and antioxidant metabolites in vital organs of male albino mice, Toxicol. Reports. 5 (2018) 765–770, https://doi.org/10.1016/J.TOXREP.2018.06.006.
[14] G. Genchi, A. Carocci, G. Lauria, M.S. Sinicropi, A. Catalano, Nickel: Human Health and Environmental Toxicology, Int. J. Environ. Res. Public Health. 17 (2020) 679, https://doi.org/10.3390/ijerph17030679.
[15] R. Patel, W. Moore, J.C. Jimenez, Severe symptomatic nickel allergy following stent graft implantation requiring excision and external iliac artery reconstruction, J. Vasc. Surg. Cases, Innov. Tech. 8 (2022) 562–564, https://doi.org/10.1016/j.jvscit.2022.08.013.
[16] I. Hulka, N.R. Florido-Suarez, J.C. Mirza-Rosca, A. Saceleanu, Mechanical properties and corrosion behavior of thermally treated Ti-6Al-7Nb dental alloy, Mater 15 (2022) 3813, https://doi.org/10.3390/MA15113813. Page1520223813.

[17] A. Silva, A.H. Plaine, Electrochemical corrosion study of biomaterials: A bibliometric study based on co-word analysis, Results. Eng. 20 (2023) 101489, https://doi.org/10.1016/j.rineng.2023.101489.
[18] W. Xu, M. Chen, X. Lu, D. wei Zhang, H. preet Singh, Y. Jian-shu, Y. Pan, X. hui Qu, C. zong Liu, Effects of Mo content on corrosion and tribocorrosion behaviours of Ti-Mo orthopaedic alloys fabricated by powder metallurgy, Corros. Sci. 168 (2020) 108557, https://doi.org/10.1016/J.CORSCI.2020.108557.
[19] C.R. Woodside, P.E. King, C. Nordlund, Arc distribution during the vacuum Arc remelting of Ti-6Al-4V, Metall. Mater. Trans. B. 44 (2013) 154–165, https://doi.org/10.1007/s11663-012-9760-1.
[20] A.H. Awad, M. Saood, H.A. Aly, A.W. Abdelghany, Role of Mo and Zr additions in enhancing the behavior of new Ti–Mo alloys for implant materials, Met. Mater. Int. (2024), https://doi.org/10.1007/s12540-024-01813-7.
[21] K. Wang, G. Cao, Y. Cai, X. Zhou, C. Xu, X. Zheng, B. Zhang, Microstructure and corrosion behavior of Ti-Mo-Zr alloy fabricated by selective laser melting in simulated oral environment, Int. J. Electrochem. Sci. 19 (2024) 100829, https://doi.org/10.1016/j.ijoes.2024.100829.
[22] A. Sotniczuk, W. Chromiński, D. Kalita, H. Garbacz, C. Xie, J. Tang, B. Dou, M. Pisarek, A. Baron-Wiecheć, Ł. Kurpaska, F. Sun, K. Ogle, Effect of Zr addition on the corrosion resistance of Ti-Mo alloy in the H2O2-containing inflammatory environment, Appl. Surf. Sci. 681 (2025) 161518, https://doi.org/10.1016/j.apsusc.2024.161518.
[23] P. Chui, R. Jing, F. Zhang, J. Li, T. Feng, Mechanical properties and corrosion behavior of β-type Ti-Zr-Nb-Mo alloys for biomedical application, J. Alloys Compd. 842 (2020) 155693, https://doi.org/10.1016/j.jallcom.2020.155693.
[24] S. Ehtemam-Haghighi, H. Attar, I.V. Okulov, M.S. Dargusch, D. Kent, Microstructural evolution and mechanical properties of bulk and porous low-cost Ti–Mo–Fe alloys produced by powder metallurgy, J. Alloys Compd. 853 (2021) 156768, https://doi.org/10.1016/j.jallcom.2020.156768.
[25] H. Zhang, F. Liu, L. Fang, J. Zhong, W. Bai, Y. Yuan, M. Rong, J. Wang, L. Zhang, L. Liu, High-throughput determination of interdiffusivity and atomic mobilities in bcc Ti–Cr–Mo alloys, J. Mater. Res. Technol. 33 (2024) 620–629, https://doi.org/10.1016/j.jmrt.2024.09.111.
[26] H. Zhang, G.-H. Zhang, Influence of Ti addition on the microstructure and comprehensive properties of Mo–Cu alloy, J. Mater. Res. Technol. 30 (2024) 2833–2847, https://doi.org/10.1016/j.jmrt.2024.04.050.
[27] N. Nohira, W.-T. Chiu, M. Tahara, H. Hosoda, Microstructural changes and mechanical property response to aging heat treatment in hypereutectoid Ti–Au–Mo biomedical alloys, Mater. Sci. Eng. A. 912 (2024) 146956, https://doi.org/10.1016/j.msea.2024.146956.
[28] W.-T. Chiu, R. Hayakawa, N. Nohira, M. Tahara, T. Inamura, H. Hosoda, Correspondence of the aging behaviors and the phase constituents of the Ti-Mo-based alloys tailored by the Al and Zr additions, J. Alloys Compd. 991 (2024) 174509, https://doi.org/10.1016/j.jallcom.2024.174509.
[29] H. Zhang, N. Gao, W. Bai, M. Rong, J. Wang, L. Zhang, L. Liu, Diffusivities and atomic mobilities in bcc Ti–V–Mo alloys, CALPHAD. 83 (2023) 102633, https://doi.org/10.1016/j.calphad.2023.102633.
[30] L. Verestiuc, M.C. Spataru, M.S. Baltatu, M. Butnaru, C. Solcan, A.V. Sandu, I. Voiculescu, V. Geanta, P. Vizureanu, New Ti–Mo–Si materials for bone prosthesis applications, J. Mech. Behav. Biomed. Mater. 113 (2021) 104198, https://doi.org/10.1016/J.JMBBM.2020.104198.
[31] A.M.G. Tavares, W.S. Ramos, J.C.G. de Blas, E.S.N. Lopes, R. Caram, W.W. Batista, S.A. Souza, Influence of Si addition on the microstructure and mechanical properties of Ti–35Nb alloy for applications in orthopedic implants, J. Mech. Behav. Biomed. Mater. 51 (2015) 74–87, https://doi.org/10.1016/j.jmbbm.2015.06.035.
[32] E. Zhao, S. Sun, Y. Zhang, Recent advances in silicon containing high temperature titanium alloys, J. Mater. Res. Technol. 14 (2021) 3029–3042, https://doi.org/10.1016/j.jmrt.2021.08.117.
[33] C. Jimenez-Marcos, J.C. Mirza-Rosca, M.S. Baltatu, P. Vizureanu, Experimental research on new developed titanium alloys for biomedical applications, Bioengineering 9 (2022) 686, https://doi.org/10.3390/bioengineering9110686.
[34] C. Jiménez-Marcos, J.C. Mirza-Rosca, M.S. Baltatu, P. Vizureanu, Evaluation of the mechanical and corrosion properties of new Ti alloys for orthopedic devices, Microsc. Microanal. 30 (2024), https://doi.org/10.1093/mam/ozae044.461.
[35] A.I.W. Conshohocken, ASTM E3-11(2017); Standard guide for preparation of metallographic specimens., (2017).
[36] International Organization for Standardization, ISO 14577-1:2015 Metallic materials — Instrumented indentation..., (2015).
[37] ISO 10271:2020 - Dentistry — Corrosion test methods for metallic materials, (2020).
[38] C. Jiménez-Marcos, J.C. Mirza-Rosca, M.S. Baltatu, P. Vizureanu, Two novel Ti–Mo–Ta–Zr alloys for medical devices: their microstructure, corrosion resistance and microhardness characteristics, Mater. Chem. Phys. 334 (2025) 130511, https://doi.org/10.1016/j.matchemphys.2025.130511.
[39] ISO 16773-1-4:2016 Electrochemical impedance spectroscopy (EIS) on coated and uncoated metallic specimens, (2016).
[40] Y. Yang, Y.A. Chang, L. Tan, Y. Du, Experimental investigation and thermodynamic descriptions of the Mo–Si–Ti system, Mater. Sci. Eng. A. 361 (2003) 281–293, https://doi.org/10.1016/S0921-5093(03)00560-4.
[41] J. Li, W. Jiang, C. Xia, Y. Deng, Y. Gao, C. Yang, Microstructural evolution and subsequent mechanical properties of Ti65 titanium alloy during long-term thermal exposure, Metals. (Basel) 14 (2024) 854, https://doi.org/10.3390/met14080854.
[42] J. Zhu, A. Kamiya, T. Yamada, A. Watazu, W. Shi, K. Naganuma, Effect of silicon addition on microstructure and mechanical properties of cast titanium alloys, Mater. Trans. 42 (2001) 336–341, https://doi.org/10.2320/matertrans.42.336.
[43] Z. Jiang, X. Dai, H. Middleton, Effect of silicon on corrosion resistance of Ti–Si alloys, Mater. Sci. Eng. B. 176 (2011) 79–86, https://doi.org/10.1016/J.MSEB.2010.09.006.
[44] C. Jimenez-Marcos, J.C. Mirza-Rosca, M.S. Baltatu, P. Vizureanu, Effect of Si contents on the properties of Ti15Mo7ZrxSi alloys, Mater 16 (2023) 4906, https://doi.org/10.3390/MA16144906. Page1620234906.
[45] R.P. Kolli, A. Devaraj, A review of metastable beta titanium alloys, Metals. (Basel) 8 (2018) 506, https://doi.org/10.3390/met8070506.
[46] P.J. Bania, Beta titanium alloys and their role in the titanium industry, JOM 46 (1994) 16–19, https://doi.org/10.1007/BF03220742.
[47] S.S. Da Rocha, G.L. Adabo, G.E.P. Henriques, M.A.D.A. Nóbilo, Vickers hardness of cast commercially pure titanium and Ti-6Al-4V alloy submitted to heat treatments, Braz. Dent. J. 17 (2006) 126–129, https://doi.org/10.1590/S0103-64402006000200008.
[48] C.N. Elias, D.J. Fernandes, C.R.S. Resende, J. Roestel, Mechanical properties, surface morphology and stability of a modified commercially pure high strength titanium alloy for dental implants, Dent. Mater. 31 (2015) e1–e13, https://doi.org/10.1016/j.dental.2014.10.002.
[49] A.V. Sandu, M.S. Baltatu, M. Nabialek, A. Savin, P. Vizureanu, Characterization and mechanical proprieties of new TiMo alloys used for medical applications, Materials. (Basel) 12 (2019) 2973, https://doi.org/10.3390/MA12182973.
[50] H. Kovacı, K. Şenel, M.T. Acar, Y.B. Bozkurt, A. Çelik, Comparative investigation of structural, morphological, mechanical, tribological and electrochemical properties of TiO2 films formed on cp-Ti, Ti6Al4V and Ti45Nb alloys, Surf. Coatings Technol. 487 (2024) 131024, https://doi.org/10.1016/j.surfcoat.2024.131024.
[51] K. Shen, W. Jiang, C. Sun, Y. Wan, W. Zhao, J. Sun, Insight into microstructure, microhardness and corrosion performance of 2205 duplex stainless steel: effect of plastic pre-strain, Corros. Sci. 210 (2023) 110847, https://doi.org/10.1016/j.corsci.2022.110847.
[52] C. Jiménez-Marcos, J.C. Mirza-Rosca, M.S. Baltatu, P. Vizureanu, Evaluation of new titanium alloys as potential materials for medical devices, Microsc. Microanal. 29 (2023) 196–201, https://doi.org/10.1093/micmic/ozad067.088.
[53] ASTM-Standards, Standard practice for calculation of corrosion rates and related information from electrochemical measurements, astm G 102 - 23. (2023) 1–3. https://doi.org/10.1520/G0102-23.
[54] F. Almeraya-Calderón, J.M. Jáquez-Muñoz, M. Lara-Banda, P. Zambrano-Robledo, J.A. Cabral-Miramontes, A. Lira-Martínez, F. Estupinán-López, C. Gaona Tiburcio, Corrosion behavior of titanium and titanium alloys in ringer's solution, Int. J. Electrochem. Sci. 17 (2022) 220751, https://doi.org/10.20964/2022.07.55.
[55] B.A. Boukamp, A nonlinear Least squares fit procedure for analysis of immittance data of electrochemical systems, Solid. State Ion. 20 (1986) 31–44, https://doi.org/10.1016/0167-2738(86)90031-7.